Particle-in-cell simulation method for macroscopic degenerate plasmas

D. Wu [1,2,*] W. Yu,[3] S. Fritzsche [4] and X. T. He[1,2,5]

[1]*Institute for Fusion Theory and Simulation, Department of Physics, Zhejiang University, 310058 Hangzhou, China*
[2]*Collaborative Innovation Center of IFSA, Shanghai Jiao Tong University, Shanghai 200240, China*
[3]*Shanghai Institute of Optics and Fine Mechanics, 201800 Shanghai, China*
[4]*Helmholtz Institut Jena, Theoretisch-Physikalisches Institut, Friedrich-Schiller-University, D-07743 Jena, Germany*
[5]*Key Laboratory of HEDP of the Ministry of Education, CAPT, and State Key Laboratory of Nuclear Physics and Technology, Peking University, 100871 Beijing, China*

(Received 4 December 2019; accepted 1 September 2020; published 18 September 2020)

Nowadays hydrodynamic equations coupled with external equation of states provided by quantum mechanical calculations is a widely used approach for simulations of macroscopic degenerate plasmas. Although such an approach is proven to be efficient and shows many good features, especially for large scale simulations, it encounters intrinsic challenges when involving kinetic effects. As a complement, here we have invented a fully kinetic numerical approach for macroscopic degenerate plasmas. This approach is based on first principle Boltzmann-Uhling-Uhlenbeck equations coupled with Maxwell's equation, and is eventually achieved via an existing particle-in-cell simulation code named LAPINS. In this approach, degenerate particles obey Fermi-Dirac statistics and nondegenerate particles follow the typical Maxwell-Boltzmann statistics. The equation of motion of both degenerate and nondegenerate particles are governed by long range collective electromagnetic fields and close particle-particle collisions. Especially, Boltzmann-Uhling-Uhlenbeck collisions ensure that evolution of degenerate particles is enforced by the Pauli exclusion principle. The code is applied to several benchmark simulations, including electronic conductivity for aluminium with varying temperatures from 2 eV to 50 eV, thermalization of alpha particles in a cold fuel shell in inertial confinement fusion, and rapid heating of solid sample by short and intense laser pulses.

DOI: 10.1103/PhysRevE.102.033312

I. INTRODUCTION

Modeling macroscopic degenerate plasmas is among the key investigation efforts for high energy density physics studies, which is of significant importance to inertial confinement fusion (ICF), astrophysics, laboratory astrophysics, and industry applications, for example, compression of the cold fuel and capsule shell [1–3], formation and evolution of white dwarf stars [4], and high power laser solid interaction experiments [5–8].

Nowadays, the density functional theory–molecular dynamics (DFT-MD) method [9–14] has been intensively investigated for degenerate plasmas. This method is thought to be accurate. However, due to significant computational expense, it is limited to certain problems it can be applied to. For macroscopic plasmas, hydrodynamic simulation [15,16] coupled with external equation of states provided by DFT-MD calculations is usually taken. Although such an approach is proven to be efficient and shows many good features, especially for large scale simulations, it encounters intrinsic challenges when plasmas depart significantly from an equilibrium state, for example, intense laser matter interaction and the stopping of energetic alpha particles in ICF research.

The particle-in-cell (PIC) method [17] has established itself as a state-of-the-art method for solving problems in kinetic plasma physics. It is a compromise between fundamental quantum mechanical simulations, i.e., DFT-MD, and macrofield only methods, i.e., hydrodynamic simulations. The main advantages of the PIC method are that their memory consumption increases linearly with the simulated volume and that the runtime is only of order N. They are also very suitable for the use of large multiprocessor systems. Although the present PIC method is very successful in a great variety of research branches, when referring to degenerate plasmas, tremendous challenges still remain. For degenerate plasmas, usually, the electron density is more than solid density. The main disadvantages of the PIC method are high noise levels and high computational requirements for plasmas at or above solid densities. Within simulations, plasma frequency needs to be resolved, and the grid size must be comparable to the Debye length in order to minimize artificial grid heating and suppress numerical instabilities. In addition to tremendous simulation burdens, degenerate particles are no longer regarded as classically distinguishable, and they obey Fermi-Dirac statistics. However, whether the PIC method based on classically distinguishable macroparticles is able to manipulate Fermi-Dirac degenerate plasmas is still open.

On the positive side, higher order interpolation algorithms have long been utilized in the explicit PIC method, which is, to some extent, successful in suppressing artificial grid

*dwu.phys@zju.edu.cn

heating and suppressing numerical instabilities. However, for degenerate plasmas, usually the electron density can be as high as 10^{24} cm^{-3}, but challenges still remain for high order explicit PIC methods. Recently, we proposed a high order interpolation implicit PIC method for plasma simulations at solid densities [18,19]. This is achieved by combining a high-order scheme of special difference with an implicit scheme of temporal stepping. This new scheme can completely remove the numerical self-heating and significantly reduce the simulation burden when simulating solid density plasmas.

At or above solid densities, when the temperature is lower than the Fermi temperature, degeneracy effect appears. Actually this effect has long been noticed in PIC simulations for solid density plasmas. For example, to avoid a divergence of the Spitzer collision frequency in cold plasma, Sentoku [20] set a threshold of plasma temperature $T_{\rm tr}$ for a degenerate plasma. Collision frequency with temperature less than $T_{\rm tr}$ is cut off with a constant value. However, in ICF and some astrophysics studies, the Fermi temperature can be as high as several hundred eV provided the plasma density is over 10^{25} cm^{-3}; a more rigorous and self-consistent approach is therefore needed.

Here in this paper, we have invented a self-consistent kinetic approach for macroscopic degenerate plasmas. This approach is based on first principle Boltzmann-Uhling-Uhlenbeck equations coupled with Maxwell's equations. This approach is eventually achieved via an existing particle-in-cell simulation code named LAPINS. With this approach, degenerate particles obey Fermi-Dirac (FD) statistics, and non-degenerate particles follow the typical Maxwell-Boltzmann (MB) statistics. The equation of motion of both degenerate and nondegenerate particles are governed by long range collective electromagnetic fields and close particle-particle collisions. Especially, the BUU collisions ensure that evolution of degenerate particles is enforced by the Pauli exclusion principle. Finally, the code is applied to several benchmark simulations, including electronic conductivity for aluminium with varying temperatures, thermalization of alpha particles in a cold fuel shell in inertial confinement fusion, and rapid heating of solid sample by short and intense laser pulses.

The paper is organized as follows. In Sec. II, we give a brief introduction of the classical framework, i.e., Boltzmann equations coupled with Maxwell's equations. In Sec. III, the semiclassical counterpart, i.e., BUU equations coupled with Maxwell's equations, is outlined. Section IV is the numerical implementation part. In Sec. V, we display several numerical experiments to benchmark this new approach. Finally, summary and discussion are given in Sec. VI.

II. CLASSICAL FRAMEWORK

In the classical framework, plasmas consisting of electrons and ions are modeled by distribution functions f_k of seven variables, i.e., the position $\mathbf{r}$, velocity $\mathbf{u}$, and time t. The distribution function f_k gives the probability $f_k(\mathbf{r},\mathbf{u},t)d\mathbf{r}\,d\mathbf{u}$ of finding particles of k species in a given volume of six-dimensional phase space $d\mathbf{r}\,d\mathbf{u}$. The electrons and ions in plasma under consideration interact via long range electromagnetic fields and close binary collisions. Hence an appropriate description of plasmas is the following Boltzmann equation:

$$\frac{\partial f_k}{\partial t}+\mathbf{u}_k\cdot\frac{\partial f_k}{\partial \mathbf{r}}-\frac{q_k}{m_k}(\mathbf{E}+\mathbf{u}_k\times\mathbf{B})\cdot\frac{\partial f_k}{\partial \mathbf{u}_k}=\frac{\partial f_k}{\partial t}|_{\rm coll}, \quad (1)$$

where $\mathbf{E}$ and $\mathbf{B}$ are the electric and magnetic fields from Maxwell's equations, q_k is the value of particle charge, and m_k is the particle mass. The Maxwell's equations read

$$\nabla\times\mathbf{E}=-\partial_t\mathbf{B}, \quad (2)$$

$$\nabla\times\mathbf{B}=\partial_t\mathbf{E}+2\pi\mathbf{J}, \quad (3)$$

$$\nabla\cdot\mathbf{E}=2\pi\rho. \quad (4)$$

Boltzmann equation, Eq. (1), is coupled with Maxwell's equations via charge density ρ and current density $\mathbf{J}$, defined as

$$\rho(\mathbf{r})=\sum_k q_k\int d^3u_k f_k, \quad (5)$$

$$\mathbf{J}(\mathbf{r})=\sum_k q_k\int d^3u_k\mathbf{u}_k f_k. \quad (6)$$

In Eq. (1), $\partial f_k/\partial t|_{\rm coll}$ represents the close collision, which is usually of the form

$$\left.\frac{\partial f}{\partial t}\right|_{\rm coll}=\int d^3p_2\int d^3p_3\int d^3p_4 W(\mathbf{p}_1,\mathbf{p}_2;\mathbf{p}_3,\mathbf{p}_4)\times\{f(\mathbf{r}_3,\mathbf{p}_3)f(\mathbf{r}_4,\mathbf{p}_4)-f(\mathbf{r}_1,\mathbf{p}_1)f(\mathbf{r}_2,\mathbf{p}_2)\}, \quad (7)$$

where $W(\mathbf{p}_1,\mathbf{p}_2;\mathbf{p}_3,\mathbf{p}_4)$ is the collision rate and the explicit form of W strongly depends on plasma conditions, e.g., temperatures and densities. The collision integral takes into account all possible two-particle scattering events: the two particles that have originally the momenta $(\mathbf{p}_1^{\rm in},\ \mathbf{p}_2^{\rm in})$ scatter into the momenta $(\mathbf{p}_3^{\rm out},\ \mathbf{p}_4^{\rm out})$ and by symmetry processes starting with $(\mathbf{p}_3^{\rm in},\mathbf{p}_4^{\rm in})$ and ending in $(\mathbf{p}_1^{\rm out},\mathbf{p}_2^{\rm out})$.

As an alternative solution of coupled Eqs. (1)–(6), plasma physicists have developed the PIC method, and this method is a Euler-Lagrange approach based on mean-field approximations. Here, particles continuously propagate over the whole phase space, while field quantities, like charge density, current density, and electromagnetic fields, are defined on fixed spacial grids. The interaction of continuously changing particles and spacial fixed fields is achieved via the interpolation technique. Such an approach significantly decreases the calculation burden by orders of magnitudes when compared with the direct numerical solution of the above coupled equations. Therefore, PIC methods make it possible to simulate large-scale plasmas even in three dimensional geometries.

As the PIC method is based on mean-field approximation, typically this method is usually applied to collisionless plasmas, where only the collective electromagnetic fields are taken into account. In order to include the close particle-particle interactions, Takizuka and Abe [21] used to proposed a Monte Carlo (MC) approach for collisions, and this PIC/MC approach is proven to be equivalent to the collision integral as shown in Eq. (7). In this approach, particles are randomly paired with each other in close proximity and scattered with Coulomb collisions, each one of which conserves energy and momentum. Apart from conservation, the greatest strength of

this approach is the ability to work with any velocity distributions, especially those which depart appreciably from MB distributions.

III. SEMICLASSICAL COUNTERPART

Equations (1)–(7) are a very general framework for classical plasma systems and hae been used very successfully during the recent half a century. However, for high energy density plasmas, especially for those that quantum effects are of significant importance, these equations are no longer applicable. In many situations however, the full quantum treatment is very involved and further approximations are desirable for the sake of simplicity. In particular, a semiclassical description of the system can provide a dramatic simplification.

In reality, with certain modifications, Eqs. (1)–(7) have been extensively applied to dense fermion systems, such as atomic nuclei [22,23], semiconductors [24], helium droplets [25], or metal clusters [26–28]. It is shown the Pauli exclusion principle plays an important role in such systems. For plasmas of high density and low temperature, FD statistics has to be built in. This leads to the BUU equations, which have found widespread applications, e.g., in nuclear physics [22,23]. The main difference between Boltzmann and BUU equations lies in the collision term,

$$\left.\frac{\partial f}{\partial t}\right|_{\text{coll}}^{\text{BUU}} = \int d^3p_2 \int d^3p_3 \int d^3p_4 W(\mathbf{p}_1, \mathbf{p}_2; \mathbf{p}_3, \mathbf{p}_4) \times \left(f_{1,2}^{\text{out}} f_{3,4}^{\text{in}} - f_{1,2}^{\text{in}} f_{3,4}^{\text{out}}\right), \tag{8}$$

where $f_{ij}^{\text{in}} = f_i f_j$ and $f_{kl}^{\text{out}} = (1 - f_k)(1 - f_l)$, with the short notation $f_i = f(\mathbf{r}_i, \mathbf{p}_i, t)$. The Pauli exclusion principle shows up explicitly here in these blocking terms, imposing that f should be less than 1 (or 2 if spin is taken into account). Namely, no more than one fermion can occupy a phase space cell of volume $(2\pi\hbar)^3$. Although the BUU collision term looks conceptually straightforward, it is technically very demanding as can be seen from the implied ninefold integration. Manageable schemes have been designed by using test particle representation of the BUU equations; for details refer to Refs. [29,30]. Therefore, in principle, the modern PIC method, when following the spirit of Refs. [29,30], can be well extended to degenerate plasmas.

Here, people may argue that it is unreasonable to define an $f = f(\mathbf{r}, \mathbf{p}, t)$ quantum mechanically because the uncertainty principle makes it impossible to simultaneously specify the position and momentum of a particle. However, we are not interested in specifying the position of any particle with accuracy much greater than the wavelength of the disturbance. Therefore, when the disturbance varies only over macroscopic distances we can specify the momentum of the particles with microscopic accuracy.

IV. NUMERICAL IMPLEMENTATION

Actually, by using the PIC method, the BUU equations are only marginally more complicated when compared to classical Boltzmann equations. However, it includes significant quantum features, like FD statistics and the Pauli exclusion principle.

A. Fermi-Dirac statistics of electrons

For degenerate electrons, under thermal equilibrium, the solution of the BUU equation is a FD function,

$$f_e(E) = \frac{(2m_e)^{3/2}}{2n_e\hbar^3\pi^2} \frac{\sqrt{E}}{\exp(E/T_e - \eta) + 1}, \tag{9}$$

where η is the degeneracy parameter and $f_e(E)dE$ is the probability for finding electrons with energy between E and $E + dE$. Degeneracy parameter η can be obtained by equation normalization,

$$\int \frac{(2m_e)^{3/2}}{2n_e\hbar^3\pi^2} \frac{\sqrt{E}\, dE}{\exp(E/T_e - \eta) + 1} = 1. \tag{10}$$

Here, Eq. (10) defines η as a function of n_e and T_e. The occupancy function is the measure of the proportion of states occupied at energy E and is given by

$$f_o(E) = f_e(E)/g_e(E) = \frac{1}{\exp(E/T_e - \eta) + 1}, \tag{11}$$

where $g_e(E) = (2m_e)^{3/2}\sqrt{E}/2n_e\hbar^3\pi^2$ is the density of states between E and $E + dE$.

When increasing temperature and decreasing density, we have $\eta = -\infty$. This is the classical limit in which the distribution functions become MB distributions.

In the low temperature and high density limit, we have $\eta = E_F/T_e$ and $\eta = \infty$, with $E_F = (3\pi^2 n_e)^{2/3}\hbar^2/2m_e$ of the Fermi energy. This is the fully degenerate limit, in which all particles are at energies below or equal to the Fermi energy. The occupancy function becomes a step function: $g(E) = 1$ with $E \leqslant E_F$ and $g(E) = 0$ with $E > E_F$. Note, in the case of the FD distribution, particles retain an energy even in the $T_e = 0$ limit.

Just as the classical PIC method, a FD distribution can be interpolated by using macroparticles. The only difference here is that, before computing the energy values in order to put particles, degeneracy parameter η in Eq. (9) needs to be solved out in advance. Given initial temperature T_e and electron density n_e in Eq. (10), the calculation of η can be done only by using the numerical method. Here in the LAPINS code, a golden section search method [31] is used for the minimization of the root sum square and calculation of η.

When implemented, as shown in Fig. 2, we have plotted the energy distribution of free electrons for solid aluminium at $T_e = 1$ eV, $T_e = 5$ eV, and $T_e = 10$ eV, respectively. Distributions generated via FD statistics are displayed by triangles and via MB statistics are displayed by diamonds. For solid aluminium, with density 2.7 g/cc, the average ionization degree is $\bar{Z} = 3$ at room temperature, and the free electron density can be as high as 1.8×10^{23} cm^{-3}. Following Eq. (10), the Fermi energy is $E_F = 11.2$ eV. As shown in Fig. 1, when temperature is well below Fermi energy, FD distributions significantly depart from MB distributions, and states with energies lower than Fermi energy are fully occupied. When temperature is well above Fermi energy, FD distributions become close to the MB distributions. Actually, at high temperatures with $T_e \gg E_F$, FD statistics will become identical to MB statistics, and the proportion of states occupied with any energy E is close to zero.

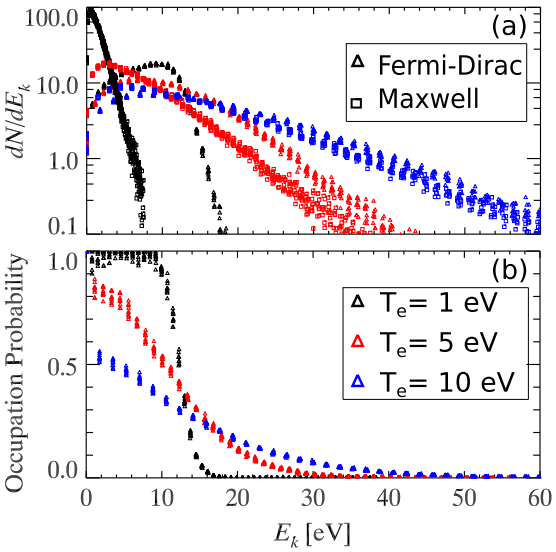

FIG. 1. LAPINS PIC code generating a Fermi-Dirac distribution of free electrons for solid density aluminium at $T_e = 1$ eV, $T_e = 5$ eV, and $T_e = 10$ eV, respectively. (a) MB and FD distributions are shown with the same parameters. (b) The occupation function sampled from the simulation distribution function.

B. BUU collisions

In fact, the finite resolution of any numerical realization causes a gradual thermalization of FD distribution towards a BM equilibrium. To prevent this, we adopt the BUU collisions, which lead to changes in energies of degenerate particles that must be constrained by the Pauli exclusion principle. This principle prevents degenerate particles being scattering into an energy state if that state is already occupied. The occupancy function, Eq. (11), is the measure of the proportion of states occupied at energy E. As $f_o(E)$ takes values between 0 and 1, from the point of view of PIC/MC simulations, it indicates whether a particular energy changing action should be blocked or not. The probability of accepting a change to final energy should be $1 - f_o(E)$; therefore, fully occupied states admit no more particles. The probability of accepting a new energy change depends on the degeneracy; therefore, for the classical limit, as $f_o(E) \to 0$ is reproduced for any E, the blocking is no longer significant.

As reflected in Eq. (11), f_o depends on the local distribution function. Within PIC/MC simulations, the local distribution function can be generated by collecting all particles within a computational cell. In order to generate a smooth f_o as a function of particle energy, the number of particles in each cell should be on the order of magnitudes 10^3 or even larger. A typical PIC simulation having 10^3 particles in each cell will quickly become computationally intractable. To avoid such an incredible simulation burden and simultaneously generate a smooth distribution or occupation function, we propose here a twofold interpretation method.

The schematic presentation of this twofold interpretation method is displayed in Fig. 2. Attaching each computational cell, we define an array with a length, for example, $n = 50$. This array is used to contain the local distribution function of degenerate particles. The cutoff energy here is defined as, for example, $E_c = 2E_F$, where $E_F = (3\pi^2 n_e)^{2/3}\hbar^2/2m_e$ is the Fermi energy. Note, this cutoff energy E_c is a global constant. Once initially defined, it is shared by each array during the entire simulation duration. The array index is therefore defined as $E_k = kd_E$, with $k \in [0, n]$ and $d_E = E_c/n$. Within PIC simulations, for a degenerate particle with an arbitrary weight w, only if the particle's energy is located within $0 < E < E_c$, the particle is used to fill an array: locating the nearest two indexes, k and $k + 1$, with $E_k < E < E_{k+1}$, and then filling them with $F_k = w(1 - \delta)S(\mathbf{r} - \mathbf{R})$ and $F_{k+1} = w\delta S(\mathbf{r} - \mathbf{R})$. Here, $\delta = (E - kd_E)/d_E$ and $S(\mathbf{r} - \mathbf{R})$ is the particle shape function, with which $\sum_{i,j,k} S[\mathbf{r} - (i\mathbf{x} + j\mathbf{y} + k\mathbf{z})] = 1$ is satisfied. Note the particle shape function used here shares the same idea with the interpolation algorithm for current assignment and force interpolation widely used in PIC codes. We find a high order interpolation algorithm along with spatial smoothing is useful in order to suppress numerical noises. This twofold interpretation method could significantly avoid an incredible simulation burden by using less particles per cell and simultaneously generate a smooth distribution or occupation function.

In PIC simulations, there is a straightforward way to achieve BUU collisions or include the Pauli exclusion principle on degenerate particles. Following the idea of Turrell [30], a Pauli block scheme is built. With the final energy E_f, a random number R is generated with $R \in (0, 1)$. For two-fermion processes, such as electron-electron scatterings, with finial energies E_{f1} and E_{f2}: block the change, if $R < f_o(E_{f1}) + f_o(E_{f2}) - f_o(E_{f1}) \cdot f_o(E_{f2})$. As a general extension, we always set $f_o(E_f) = 0$ for nondegenerate particles. For single fermion processes, such as electron-ion scattering, block the change if $R < f_o(E_f)$; accept the change if $R > f_o(E_f)$. In the classical limit, $f_o(E) \to 0$ for any E_f, changes in particle energy are rarely blocked.

In order to benchmark the implemented BUU collisions, we take PIC calculations for the same sample as displayed in Fig. 1. The simulation box is divided into $10 \times 10 \times 10$ computational cells bounded by periodic conditions, with each cell containing 100 macroelectrons. Here, energy distribution of free electrons for solid aluminium with $T_e = 1$ eV is displayed in Fig. 3. As shown in Fig. 3(a), an initial FD distribution

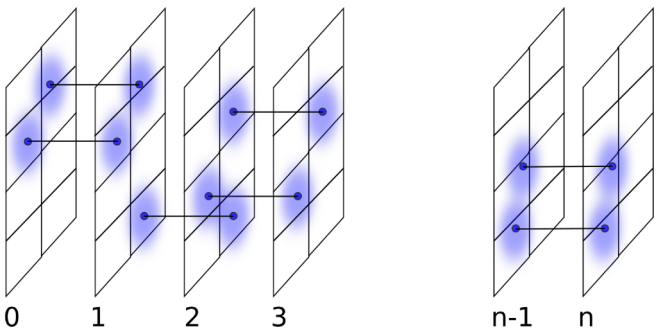

FIG. 2. Schematic presentation of the twofold interpretation method. Here, n is the length of array containing distribution functions and see text for further explanations. In this plot, the shape function of particle is represented here by a blue 2D circular particle shape and spatial 2D grids are presented by black lines. Note, for 3D simulation, 3D particle shape and spatial grids are used instead.

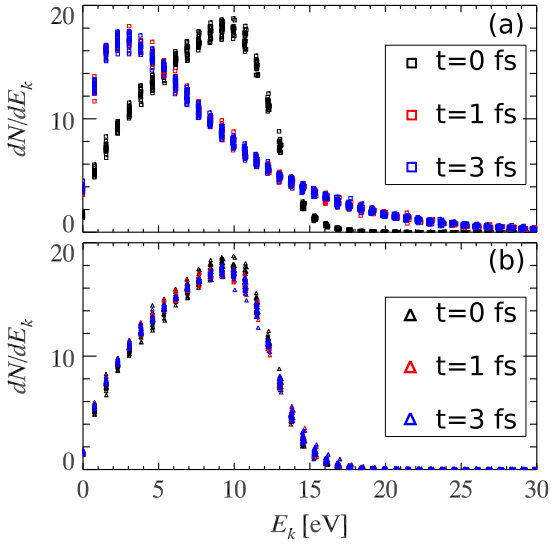

FIG. 3. (a) With an initial FD distribution, it relaxes to a MB distribution after 1 fs. (b) With an initial FD distribution, when including Pauli exclusion principle, it sustains within the entire simulation duration. Simulation sample is the same as displayed in Fig. 1. The temperature of aluminium plasma is $T_e = 1$ eV.

relaxes to a MB distribution after only 1 fs. However, when taking into account the Pauli exclusion principle, as shown in Fig. 3(b), FD distribution is sustained within the entire simulation duration. Note, the simulation speed is only slightly affected by including the Pauli exclusion principle. This is because the same interpretation method is used throughout the code for both current assignment and force interpretations.

C. Modification of collision rate

In practical implementation, the Monte Carlo binary collision model requires knowledge of the collision rate W, as shown in Eq. (7). Its explicit form strongly depends on the momentum transfer cross section, which is a function of plasma temperature and densities. In degenerate plasmas, such a cross section significantly differs from classical plasmas.

Seriously, in the partial wave calculation [32], this momentum transfer cross section can be obtained by numerical solution of the Schrödinger equation for a well defined potential. In the original work of Lee and More [33], the Thomas-Fermi potential was taken as an approximate candidate. Recently, a more rigorous approach has been proposed by Starrett [32] that includes correlations with electrons and ions surrounding the central scatterer through the quantum fluid equations. Although it is possible to use a tabulated cross section via machine-learning methods or others, here in the present LAPINS code, we still use the screened Coulomb cross section with approximate cutoff parameters. This is because our goal is to invent a simulation method for degenerate plasmas for practical applications, and we need a simple yet approximately accurate method for calculating cross sections.

One of the practical approaches for classical Coulomb cross section calculation, as used by Takizuka [21] and Sentoku [20], is to sum binary collisions over a distance of the order of the Debye length. Under the Coulomb potential of $1/r$, the differential cross section reads

$$\sigma(\theta) \sim 1/\sin^4(\theta/2) \tag{12}$$

and the Coulomb logarithm reads

$$L \sim \int_0^\pi \sin\theta \, \sin^2(\theta/2)\sigma(\theta)d\theta \sim \ln[\sin(\theta/2)]|_0^\pi. \tag{13}$$

This integration is not a convergent value, when $\theta \to 0$. While in plasmas, the potential of a charged particle should be screened. When b, i.e., the minimum impact parameter, is larger than λ_D, the potential is artificially set to be zero. Therefore, the lower limit $\theta_{\min}$ of the scattering angle is obtained when $b = \lambda_D$, i.e., $\theta_{\min}/2 = b/\lambda_D$. The Coulomb logarithm is written as $L \sim \ln(\lambda_D/b)$. In this model, for degenerate plasmas with b close to or even larger than λ_D, the Coulomb logarithm is artificially cut off to a value equal to 2.0.

Instead of the above method, a better approach is to sum binary collisions with all surrounding particles using the screened potential $\exp(-r/\lambda_D)/r$. Acting on this screened potential, under Born approximation, the differential cross section can be analytically obtained with

$$\sigma(\theta) \sim 1/[\sin^2(\theta/2) + \xi]^2, \tag{14}$$

where ξ is noting but the ratio of minimum impact parameter and the Debye length $\xi = b_{\min}/\lambda_D$. The minimum impact parameter is set by the classical distance of the closest approach. This gives

$$b_{\min} = Z_a Z_b e^2/m_{ab}u_{ab}^2. \tag{15}$$

Here, Z_a and Z_b are the charge number of particle a and particle b; m_{ab} and u_{ab} are their reduced mass and relative velocity. However, at high energy, $b_{\min}$ is set by the uncertainty principle. We have

$$b_{\min} = \lambda/2 = \hbar/m_{ab}u_{ab}. \tag{16}$$

Here λ is the de Broglie wavelength. The Coulomb logarithm $L \sim \int_0^\pi \sin\theta \, \sin^2(\theta/2)\sigma(\theta)d\theta$ by applying the new differential cross section is integrable with

$$L \sim \ln[1 + 2\eta - \cos(\theta)]|_0^\pi \sim \ln[(1+\eta)/\eta]. \tag{17}$$

This expression of Coulomb logarithm will converge to $L = \ln(\lambda_D/b)$ at the classical limit with $b \ll \lambda_D$. For degenerate plasmas, this expression of Coulomb logarithm reduces to zero.

In our model, the screening is only determined by the Debye length. This length, following Debye-Huckel theory, can be written as

$$\frac{1}{\lambda_D^2} = \frac{4\pi n_e e^2}{kT_e} + \frac{4\pi n_i e^2 \bar{Z}^2}{kT_i}, \tag{18}$$

where T_e and T_i are the electron and ion temperature, n_e and n_i are the electron and ion density, and $\bar{Z}$ is the average ionization degree. Note, the ion contribution is dominant for plasmas containing heavy atoms. The degeneracy correction [34] to the screening is to multiply the first term on the right hand of Eq. (18) by a factor $F'_{1/2}/F_{1/2}$, i.e., the logarithm of derivative of the Fermi integral,

$$F_j(x) = \int_0^\infty \frac{x^j dx}{1 + \exp(x - \eta)}, \tag{19}$$

where η is the degeneracy parameter defined by Eq. (10). The second term remains unchanged. According to the original work of Brysk, Campbell, and Hammerling [35], such a degeneracy correction can be approximated to

$$\frac{1}{\lambda_D^2} = \frac{4\pi n_e e^2}{\left(T_e^2 + E_F^2\right)^{1/2}} + \frac{4\pi n_i e^2 \bar{Z}^2}{T_i}. \tag{20}$$

This approximation matches the numerical calculation of the factor $F'_{1/2}/F_{1/2}$ within 5%, giving negligible error in the logarithm.

For electrons of FD distributions, diagnosing the electron temperature is nontrivial. Here, the average electron energy is

$$\bar{E} = \frac{3\sqrt{\pi}}{8}\frac{T_e}{n_e}\frac{(2m_e T_e)^{3/2}}{\hbar^3\pi^2}F_{3/2}(\eta). \tag{21}$$

At classical limit, $\bar{E} = (3/2)T_e$, and at quantum limit, $\bar{E} = (3/5)E_F$. Within PIC simulations, Eq. (21) can be approximated by $\bar{E} \sim \bar{E}_{\rm PIC} = \sum_i w_i\epsilon_i / \sum_i w_i$, where ϵ_i is the energy for each single macroparticle and w_i is the corresponding weight. The first term on the right hand of Eq. (20) can therefore be directly approximated as $4\pi n_e e^2/\bar{E}_{\rm PIC}$, also giving negligible error in the logarithm.

For projectile moving in the plasmas, the static Debye length needs to be replaced by the corresponding dynamical value. According to Zwicknagel [36], this dynamical Debye length reads $\tilde{\lambda}_D = \lambda_D(1 + m_{ab}u_{ab}^2/T_e^2)$. In the LAPINS code, this dynamical Debye length is used throughout the simulations, although we might have a small difference in the logarithmic scale. This is because having one general formula for stopping and relaxation problems is useful for practical applications, such as the laser-solid interactions, which contain both the stopping and thermalization of fast particles.

D. Modification of ionization dynamics

In the LAPINS code, the treatment of ionization is divided into two parts: field ionization [37,38] and impact ionization. As field ionization usually appears under low density plasmas, therefore, there is no need to take into account degeneracy corrections. For solid density plasmas, a dynamic ionization model was proposed by Wu [39], taking into account impact ionization, electron-ion recombination, and ionization potential depression (IPD) by the shielding of surrounding plasmas. Here, we would suggest including the degeneracy effect by correcting ionization potential with $P - \Delta P + E_F$, with P the isolated ionization potential [40], ΔP the IPD correction [41,42], and E_F the Fermi energy. As there is no space to contain the newly ionized electrons with energy lower than E_F, the minimum kinetic energy of a newly ionized electron must be higher than E_F. Numerical experiments, Fig. 4, have shown that such a degeneracy correction would slightly decrease the ionization cross section and therefore the average ionization degree when the plasma temperature is comparable with or lower than E_F.

V. BENCHMARKS AND APPLICATIONS

In this section, the quantum-LAPINS code is applied to several benchmark simulations and applications, including electronic conductivity for aluminium with varying temperatures, thermalization of alpha particles in a cold fuel shell in ICF, and rapid heating of solid sample by short and intense laser pulses.

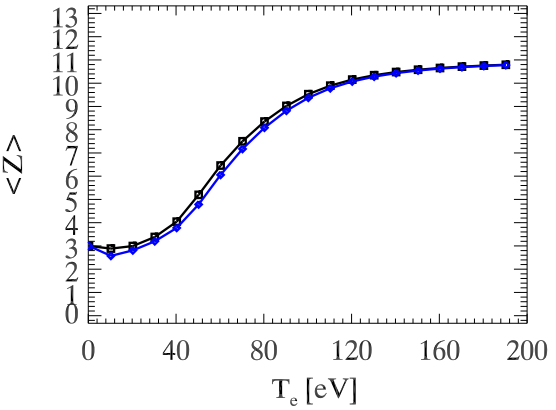

FIG. 4. Average ionization degree of solid aluminium as a function of temperature. Black square line is the one taking into account FD statistics and the Pauli exclusion principle, and blue diamond line is the one treated by classical method.

A. Electronic conductivity of aluminium

The calculation of electronic conductivity for plasmas of any degeneracy is a challenging problem. One approach is to use DFT-MD simulations coupled with Kubo-Greenwood formalism [9,10]. This approach is thought to be an accurate method for high frequency alternating current (ac) conductivity. However, the parameters widely used in both hydrodynamic and PIC simulations are conductivities at low frequency limit, i.e., the so-called direct current (dc) conductivity. For the calculation of dc conductivity, one usually refers to the Boltzmann equation with relaxation-time approximations. The question then becomes calculating the electron-ion cross sections. To calculate the electron-ion cross section of degenerate plasmas, one needs to define an electron-ion scattering potential. How this potential is made strongly affects the resulting conductivities. Recently, a new quantum potential is defined by Starrett [32]. This potential includes correlations with electrons and ions surrounding the central scatterer through quantum Ornstein-Zernike equations [43]. When coupled to the relaxation-time approximation, results indicate that relaxation-time approximation plus well defined potential could lead to quite accurate conductivity predictions when compared to DFT-MD simulations.

The underlying frame of the LAPINS code is the BUU equations coupled with the Maxwell's equations. Therefore, for electronic conductivity calculation, the relaxation-time approximation method can be naturally recovered. By placing a small external electric field on a plasma sample, free electrons are accelerated by this small electric field, and simultaneously experience collisions with surrounding ions and other electrons. When reaching steady state, the conductivity is evaluated as $\sigma = \mathbf{J}/\mathbf{E}$, with $\mathbf{J}$ and $\mathbf{E}$ of current density and the external small electric field.

In Fig. 5, we have plotted the electron current density as a function of time for a solid aluminium sample, when

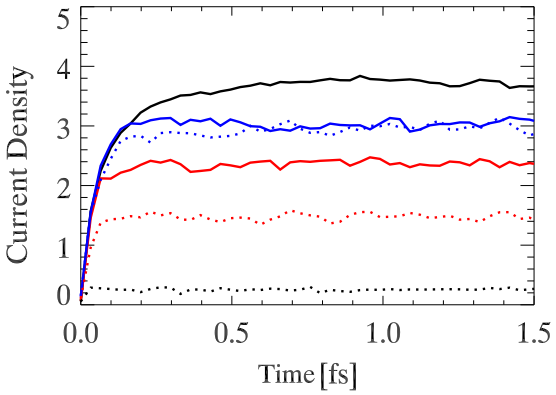

FIG. 5. Electron current density, in units of en_0c, as a function of time for a solid aluminium sample, when externally placing the same small electric field. In the simulation, with normalization, the thickness of aluminium sample is $l = 0.1$ and divided into 100 cells, with each cell containing 1000 electrons and 1000 ions. Cells are connected by periodic boundary conditions. The applied external electric field is $E_{ex} = 0.001$. Here, black, red, and blue curves are the ones with $T_e = 2$ eV, $T_e = 10$ eV, and $T_e = 20$ eV, respectively. Solid and dashed lines correspond to simulations with degeneracy and without degeneracy.

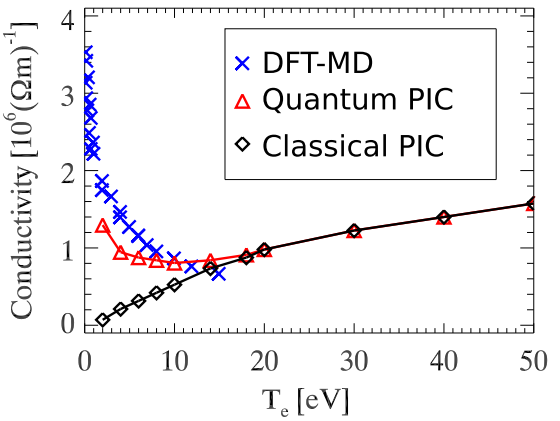

FIG. 6. Electrical conductivity of solid aluminium. Our results of quantum-PIC and classical-PIC are compared with full quantum mechanical calculations, i.e., the Kubo-Greenwood DFT-MD method from Witte [44].

externally placing a small electric field. This current density increases at initial time due to the acceleration of electrons by the electric field and then reaches saturation due to the antibalance forces from collisional scatterings. Here, black, red, and blue curves represent current density evolution at different temperatures, with $T_e = 2$ eV, $T_e = 10$ eV, and $T_e = 20$ eV, respectively. Solid and dashed lines correspond to simulations with degeneracy and without degeneracy. For classical-LAPINS (without quantum effects), the final saturation current density increases when increasing temperature. However, with $T_e < T_F$, the new quantum-LAPINS code shows increasing saturation current density when decreasing plasma temperature. This is because, under low temperature limit, the collision cross section is significantly reduced as the electrons well below the Fermi surface are hardly scattered. In Fig. 6, electronic conductivity calculated by the quantum-LAPINS code is compared with full quantum mechanical calculations, i.e., the Kubo-Greenwood DFT-MD method from Witte [44]. It is shown that the quantum-LAPINS code could generally produce accurate conductivities when compared to full quantum mechanical simulations. At high temperatures, the results of quantum and classical codes coincide with each other as expected.

B. Thermalization of alpha particles in a cold fuel shell in inertial confinement fusion

In ICF, the yield of neutrons is particularly sensitive to electron-ion equilibration. Simulations of direct-drive implosions have shown a 10% difference across several different models of temperature relaxation [45]. The distribution of fusion produced alpha particles is highly non-Maxwellian; however, the quantum-LAPINS code with the implemented collision method is capable of modeling such a complex interaction. Figures 7 and 8 show simulations with parameters

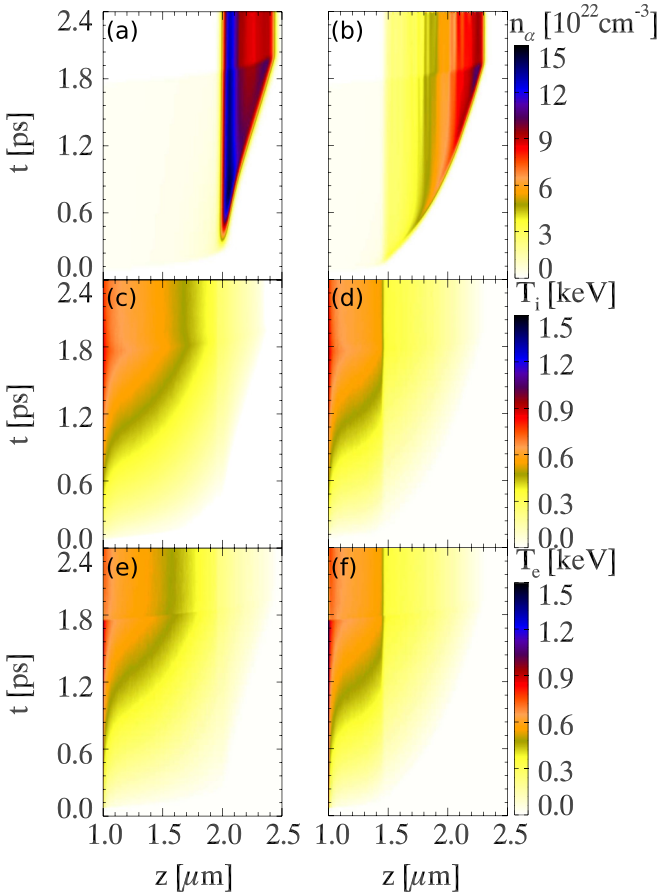

FIG. 7. With parameters approximately similar to ICF: starting temperatures of electrons, deuterium, and tritium are 10 eV; the density is $n_D = n_T = 1.5 \times 10^{24}$ cm^{-3}, $n_\alpha = 1. \times 10^{21}$ cm^{-3}, and $n_e = 3 \times 10^{24}$ cm^{-3}; α particles have an initial energy of 3.54 MeV. Evolution of alpha particle density, electron temperature, and DT temperature are displayed in (a)-(b), (c)-(d), and (e)-(f). Here (a), (c), and (e) are calculated by the quantum-LAPINS code and (b), (d), and (f) are by the classical-LAPINS code.

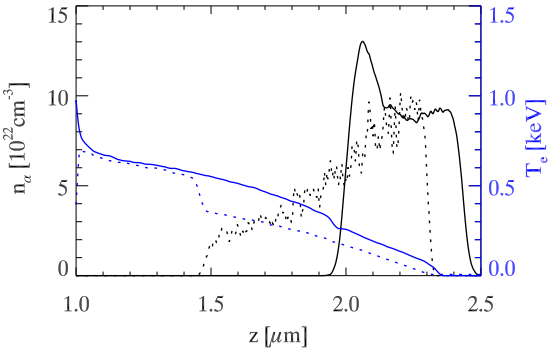

FIG. 8. Parameters are the same as displayed in Fig. 7; density of alpha particles and temperature of electrons are displayed at $t = 2.4$ ps. Solid lines are calculated by the quantum-LAPINS code and dashed lines are calculated by the classical-LAPINS code.

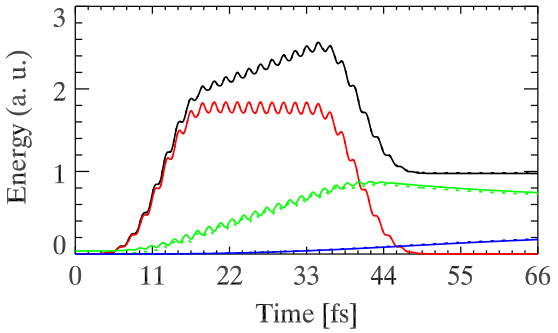

FIG. 9. Energy (transfer) as a function of time. Data are shown for laser energy entering into the simulation box (black), electromagnetic energy (red), electron kinetic energy (blue), and ionization energy (dashed). Here solid lines are obtained by the quantum-LAPINS code and dashed lines are from the classical code. Especially, the laser energy entering into the simulation box is calculated as $\sum(\mathbf{E} \times \mathbf{B})\delta y \delta t$, where δt is the time step of the simulation box. Ionization energy is a record of energy losses of plasmas, as ionization will reduce the energies of electromagnetic fields and electrons.

approximately similar to ICF: a flux of monoenergetic fusion produced alpha particles interacting with a cold fuel shell of deuterium (D), tritium (T), and electrons. In the simulation, the initial density and temperature of cold D-T plasma are 3×10^{25} cm^{-3} and 10 eV. We set the density of alpha particles to 10^{21} cm^{-3}, and we set the initial energy of alpha particles to 3.54 MeV. In the one-dimensional PIC simulation, a source of alpha particles, lasting for 1.6 ps, comes from the left simulation boundary and the particles interact with cold D plasmas, which lie within 1 μm and 3 μm. The simulation space is divided into 1200 cells, with each cell containing 1000 macroparticles. For comparison, results of classical LAPINS are also displayed.

In Fig. 7 and Fig. 8, evolution of alpha particle density, electron temperature, and DT temperature are displayed. The quantum-LAPINS simulation predicts a significantly large penetration range of alpha particles, due to the reduction of collisions by Pauli exclusion principle. Moreover, the heating zone is also significantly enlarged as predicted by the quantum-LAPINS code. Such finding would be of importance to the target design in the ICF research.

C. Rapid heating of solid sample by short and intense laser pulses

The rapid heating of solid sample by short and intense laser pulses is of significant importance to the investigation of warm dense matter in laboratories, and is also of key importance to many related applications, such as laser driven ion sources, laser driven neutron sources, and laser driven x/γ ray sources.

Here we take solid aluminium as an example. The aluminium density is 2.7 g/cc, initial temperature is at room temperature, and the thickness of the sample is 1.5 μm. The intensity of incident laser is 10^{18} W/cm^2, pulse duration is 30 fs, and laser wavelength is 1 μm.

In simulations, the simulation space is uniformly divided into grids with $\delta z = 0.01$ μm and $\delta y = 0.02$ μm. In each grid, 100 Al^{3+} ions and 300 electrons are filled initially. Within the simulations, field ionization, collision ionization, and ion-electron recombination are all taken into account.

Here, Fig. 9 shows the temporal evolution of energy (transfer) into the simulation box, including laser energy entering (black), electromagnetic field energy (red), electron kinetic energy (green), the ion kinetic energy (blue), and ionization energy (dashed), repetitively. The laser energy, entering into the simulation box, first increases, then decreases (some is reflected), and finally reaches a constant value at $t = 45$ fs. Within the interaction, there is a strong energy transfer from the electromagnetic energy to the electron-kinetic energy, and then from electron-kinetic energy to ionization energy (ionization appears). Note, in this simulation case, which only lasts for 66 fs, the ion kinetic energy is very small. This is because the mass of ion is quite large, and the energy transfer rate from electrons to ions is slow. In this plot, the solid lines represent results obtained by the quantum-LAPINS code and the dashed lines are from the classical-LAPINS code. As we can see from the energy transfer history, the difference between them is quite small. This is because, as will be shown below, under such intense laser irradiations only a minor part of the aluminium sample is in degenerate states, and degenerate effects only appear when temperature is below Fermi temperature (for aluminium it is 11 eV).

When energetic electrons transport within the solid aluminium, a self-generated electromagnetic field appears, which might significantly affect both the transport behavior of energetic electrons and the volume heating of background plasmas. Such electromagnetic fields strongly depend on resistivity and conductivity of the solid aluminium. As a comparison of the quantum-LAPINS code and the classical-LAPINS code, in Fig. 10, the self-generated electric fields are displayed, which are recorded at $t = 40$ fs. Results from quantum and classical codes are shown in Fig. 10(a) and Fig. 10(b), respectively. In Fig. 10(c), a detailed comparison between them, by slicing electric field distributions along $z = 0.7$, $z = 1.0$, $z = 1.5$, and $z = 1.7$ μm, are presented. It is shown, at $z = 0.7$ and $z = 1.0$ μm, the amplitude of the self-generated electric field calculated by the quantum-LAPINS code is quite close to the one from the classical code. This is because, as we will show below, the electron temperature at the front part of

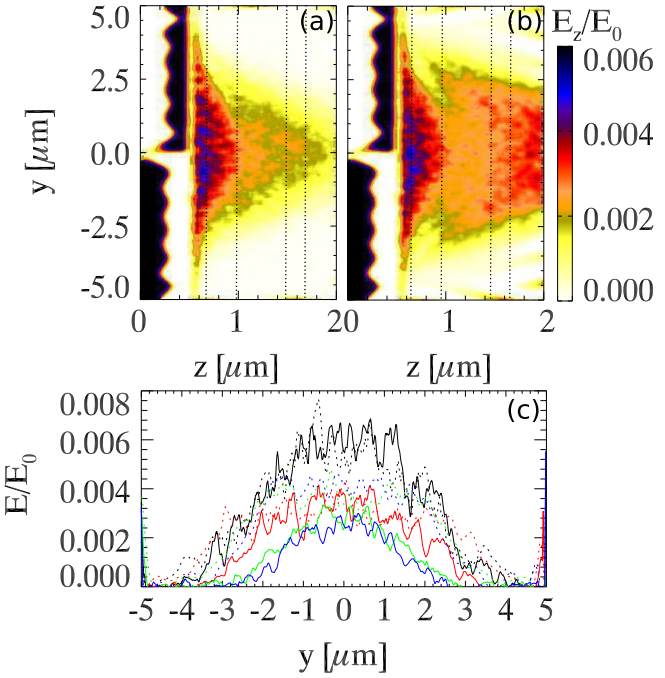

FIG. 10. Self-generated electric fields for the quantum-LAPINS code (a) and the classical-LAPINS code (b) at $t = 40$ fs. In (c), we display the electric field along the dashed line as marked in (a) or (b). Values along $z = 0.7$, $z = 1.0$, $z = 1.5$, and $z = 1.7$ μm are plotted in black, red, green, and blue, respectively. As a comparison, dashed lines in (c) are the corresponding values from the classical-LAPINS code.

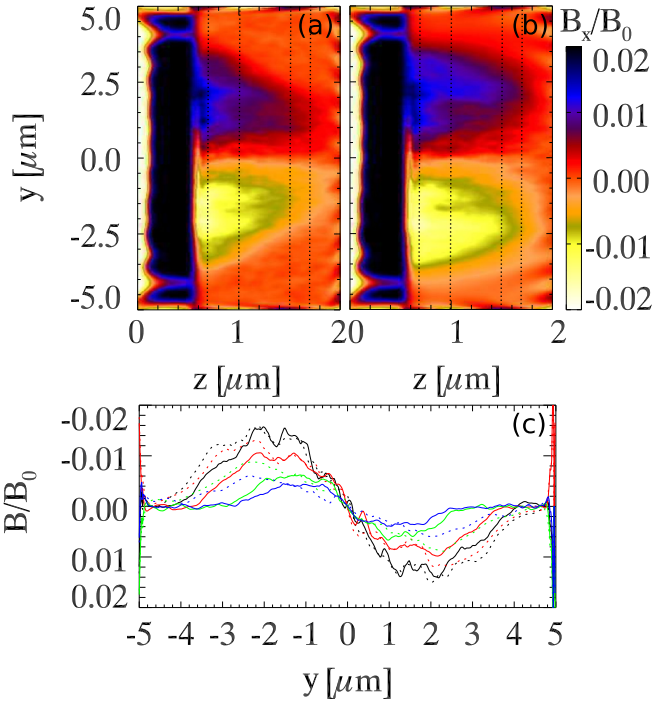

FIG. 11. Self-generated magnetic fields for the quantum-LAPINS code (a) and the classical-LAPINS code (b) at $t = 40$ fs. In (c), we display the magnetic field along the dashed line as marked in (a) or (b). Values along $z = 0.7$, $z = 1.0$, $z = 1.5$, and $z = 1.7$ μm are plotted in black, red, green, and blue, respectively. As a comparison, dashed lines in (c) are the corresponding values from the classical-LAPINS code.

the aluminium sample is significantly higher than the Fermi temperature, and the degenerate effect is therefore negligible. However, when close to the backside of the target, for example, at $z = 1.5$ and $z = 1.7$ μm, the electric fields obtained by the quantum-LAPINS code depart significantly from the classical-LAPINS code. As the forward moving energetic electrons are produced by direct laser acceleration in front of the target, it is reasonable to assume the forward moving current density, $\mathbf{J}_e$, carried by energetic electrons, are equal to each other for both quantum and classical simulations. It is also reasonable to assume the magnitude of return currents, carried by low energy background electrons, are also equal to $\mathbf{J}_e$. The resistivity, ν, in quantum code is much smaller than that in classical code, especially when the temperature is below E_F. Considering the self-generated electric fields are produced mainly by $\mathbf{E} = \nu\mathbf{J}_e$, this is the reason why the amplitude of electric field calculated by the quantum-LAPINS code is small, for example, at $z = 1.5$ and $z = 1.7$ μm, when compared with the one from the classical code.

Figure 11 shows the corresponding plots of corresponding magnetic fields at $t = 40$ fs. Similarly, results from quantum and classical codes are shown in Fig. 11(a) and Fig. 11(b), respectively. In Fig. 11(c), a detailed comparison between them, by slicing electric field distributions along $z = 0.7$, $z = 1.0$, $z = 1.5$, and $z = 1.7$ μm, are also displayed. It is shown, at $z = 0.7$ and $z = 1.0$ μm, the amplitude of self-generated magnetic field calculated by the quantum-LAPINS code is quite close to the one from the classical code. However, when close to the backside of the target, for example, at $z = 1.5$ and $z = 1.7$ μm, the magnetic fields obtained by the quantum-LAPINS code are small when compared with the classical code. This can be understood with the same reason when referring to the self-generated electric fields. As the magnetic fields and electric fields are connected by Faraday's law $\partial\mathbf{B}/\partial t = -c\nabla \times \mathbf{E}$, this is the reason why the magnetic fields obtained by the quantum-LAPINS code are small especially when close to the backside of the sample.

In Fig. 12, we have plotted the electron density and temperature at $t = 66$ fs. As the simulation containing both thermal and superhot electrons, a boundary is set at "10 keV"

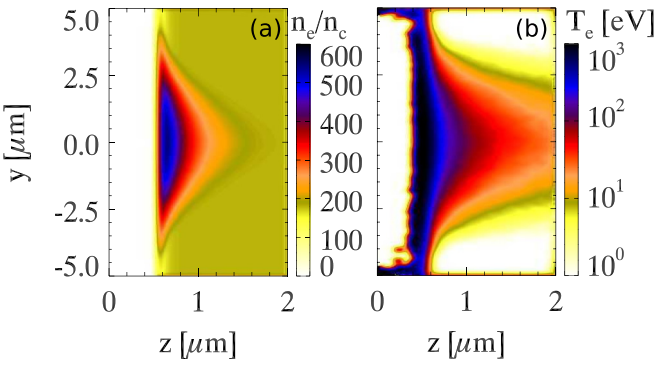

FIG. 12. Electron density (a) and electron kinetic energy density (b) at $t = 66$ fs.

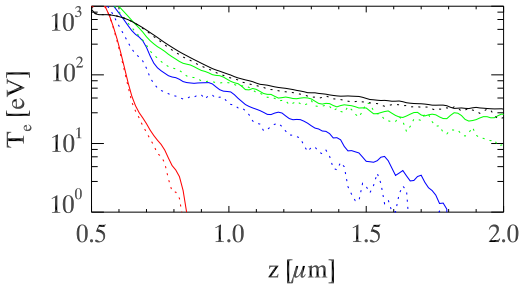

FIG. 13. Electron temperature, along the axis of $y = 0$ μm, at $t = 16$ fs (red), $t = 22$ fs (blue), $t = 25$ fs (green), and $t = 66$ fs (black), respectively. Results calculated by quantum-LAPINS are displayed in solid lines, while from classical-LAPINS are displayed in dashed lines.

to exclude superhot electrons from directly contributing to the electron temperature. In the classical-LAPINS code, the calculation of electron temperature is quite straightforward, which can be regarded as electron kinetic energy density divided by electron density. In the quantum-LAPINS code, the calculation of electron temperature is nontrivial. As suggested by Turrell [30], the method employed is first to calculate the probability density function from simulation in a number of bins. Then T_e and therefore η by Eq. (9) can be varied until the root sum of square differences between the simulation distribution and the Fermi-Dirac distribution is minimized. In Fig. 13, the electron temperatures, along the axis of $y = 0$ μm, from quantum and classical codes are compared with each other. Due to the reduced collision frequency of forward moving electrons with the background, the heating zone as predicted by the quantum-LAPINS code is apparently larger than the corresponding classical case, for example, at $t = 22$ fs (blue), $t = 25$ fs (green), and $t = 66$ fs (black).

VI. DISCUSSIONS AND CONCLUSIONS

As a semiclassical approach, the invented method is very general and can find great applications. Although FD statistics and Pauli exclusion principle have been taken into account, and this approach is able to deal with degenerate plasmas with temperature well below Fermi temperature E_F, it still misses some key features. For quantum systems, indistinguishability of quantum particles gives rise to an additional mean field–type term, i.e., the exchange contribution. Due to the finite extension of quantum particles, the exchange contribution has a complicated form (it is nonlocal). Usually, the exchange-correlation energy $V_{\rm ex}(\rho)$ can be calculated by taking the standard ansatz with the local density approximation (LDA). In practice, using the Gunnarsson-Lundqvist parametrization [46], we have

$$V_{\rm ex}(\rho) = e^2\left(\frac{3\rho}{\pi}\right)^{\frac{1}{3}} - \frac{2e^2}{30}\left\{1+\ln\left[1+11.4\left(\frac{4\pi\rho}{3}\right)^{\frac{1}{3}}\right]\right\}. \quad (22)$$

For aluminium of density 2.7 g/cc, according to Eq. (22), we have $V_{\rm ex} = 1.4$ eV at the low temperature limit. It is therefore reasonable to give an application limit of the present semiclassical approach. The quantum-LAPINS code is applicable when electron temperature is well above $V_{\rm ex}$, as displayed in Fig. 6 with a temperature floor of 2 eV. Note this is a significant improvement when compared with the classical-LAPINS code, as $V_{\rm ex}$ is usually several times smaller than E_F.

To summarize, in this paper, we have invented a self-consistent kinetic approach for macroscopic degenerate plasmas. With this approach, degenerate particles are initialized according to a Fermi-Dirac distribution function and nondegenerate particles are initialized following a typical Maxwell distribution function. The equation of motion of both degenerate and nondegenerate particles are governed by long range collective electromagnetic fields and close particle-particle scatterings with degeneracy corrections. Especially, evolution of degenerate particles is also constrained by the Pauli exclusion principle. The new code might find great applications in ICF, astrophysical, and laboratory astrophysical studies. The method invented in this paper is applicable for degenerate plasmas, but with a limitation that the electron temperature should be well above $V_{\rm ex}$.

ACKNOWLEDGMENTS

One of the authors, D.W., would like to thank H. Xu and W. M. Wang for fruitful discussions. This work was supported by the Strategic Priority Research Program of Chinese Academy of Sciences (Grant No. XDA250050500) and Science Challenge Project (No. TZ2016005).

[1] J. Lindl, Phys. Plasmas **2**, 3933 (1995).
[2] Y. Setsuhara, H. Azechi, N. Miyanaga, H. Furukawa, R. Ishizaki, K. Nishihara, M. Katayama, A. Nishiguchi, K. Mima, and S. Nakai, Laser Part. Beams **8**, 609 (1990).
[3] X. T. He, J. W. Li, Z. F. Fan, L. F. Wang, J. Liu, K. Lan, J. F. Wu, and W. H. Ye, Phys. Plasmas **23**, 082706 (2016).
[4] J. P. Cox and R. T. Giuli, *Principles of Stellar Structure Volume II: Applications to Stars* (Gordon and Breach Science Publishers, New York, 1968).
[5] F. N. Beg, A. R. Bell, A. E. Dangor, C. N. Danson, A. P. Fews, M. E. Glinsky, B. A. Hammel, P. Lee, P. A. Norreys, and M. Tatarakis, Phys. Plasmas **4**, 447 (1997).
[6] P. K. Patel, A. J. Mackinnon, M. H. Key, T. E. Cowan, M. E. Foord, M. Allen, D. F. Price, H. Ruhl, P. T. Springer, and R. Stephens, Phys. Rev. Lett. **91**, 125004 (2003).
[7] W. Bang, B. J. Albright, P. A. Bradley, E. L. Vold, J. C. Boettger, and J. C. Fernandez, Phys. Rev. E **92**, 063101 (2015).
[8] G. M. Dyer, A. C. Bernstein, B. I. Cho, J. Osterholz, W. Grigsby, A. Dalton, R. Shepherd, Y. Ping, H. Chen, K. Widmann, and T. Ditmire, Phys. Rev. Lett. **101**, 015002 (2008).
[9] M. P. Desjarlais, J. D. Kress, and L. A. Collins, Phys. Rev. E **66**, 025401(R) (2002).
[10] T. Sjostrom and J. Daligault, Phys. Rev. E **92**, 063304 (2015).

[11] B. Holst, M. French, and R. Redmer, Phys. Rev. B **83**, 235120 (2011).
[12] M. French and T. R. Mattsson, Phys. Rev. B **90**, 165113 (2014).
[13] S. X. Hu, L. A. Collins, T. R. Boehly, J. D. Kress, V. N. Goncharov, and S. Skupsky, Phys. Rev. E **89**, 043105 (2014).
[14] M. P. Desjarlais, C. R. Scullard, L. X. Benedict, H. D. Whitley, and R. Redmer, Phys. Rev. E **95**, 033203 (2017).
[15] M. R. Krumholz, R. I. Klein, and C. F. McKee, Astrophys. J. **754**, 71 (2012).
[16] N. Higginbottom, C. Knigge, K. S. Long, J. H. Matthews, S. A. Sim, and H. A. Hewitt, Mon. Not. R. Astron. Soc. **479**, 3651 (2018).
[17] C. K. Birdsall and A. B. Langdon, *Plasma Physics via Computer Simulation* (Taylor and Francis, New York, 2005).
[18] D. Wu, W. Yu, S. Fritzsche, and X. T. He, Phys. Rev. E **100**, 013207 (2019).
[19] D. Wu, W. Yu, Y. T. Zhao, D. H. H. Hoffmann, S. Fritzsche, and X. T. He, Phys. Rev. E **100**, 013208 (2019).
[20] Y. Sentoku and A. J. Kemp, J. Comput. Phys. **227**, 6846 (2008).
[21] T. Takizuka and H. Abe, J. Comput. Phys. **25**, 205 (1977).
[22] G. F. Bertsch and S. Das Gupta, Phys. Rep. **160**, 189 (1988).
[23] A. Bonasera, F. Gulminelli, and J. Molitoris, Phys. Rep. **243**, 1 (1994).
[24] R. Brout and P. Carruthers, *Lectures on the Many-Electron Problem* (Wiley, New York, 1963).
[25] M. Guilleumas, M. Pi, M. Barranco, and E. Suraud, Z. Phys. D **34**, 35 (1995).
[26] M. Gross and C. Guet, Z. Phys D **33**, 289 (1995).
[27] L. Feret, E. Suraud, F. Calvayrac, and P. G. Reinhard, J. Phys. B **29**, 4477 (1996).
[28] M. Gross and C. Guet, Phys. Rev. A **54**, R2547 (1996).
[29] A. Domps, P.-G. Reinhard, and E. Suraud, Ann. Phys. (NY) **260**, 171 (1997).
[30] A. E. Turrell, M. Sherlock, and S. J. Rose, J. Comput. Phys. **249**, 13 (2013).
[31] W. H. Press, S. A. Teukolsky, W. T. Vetterling, and B. P. Flannery, *Numerical Recipes in* C + + (Cambridge University Press, Cambridge, UK, 2007).
[32] C. E. Starrett, High Energy Density Phys. **25**, 8 (2017).
[33] Y. T. Lee and R. M. More, Phys. Fluids **27**, 1273 (1984).
[34] E. E. Salpeter, Aust. J. Phys. **7**, 373 (1954).
[35] H. Hrysk, P. M. Campbell, and P. Hammerling, Plasma Phys. **17**, 473 (1975).
[36] G. Zwicknagel, C. Toepffer, and P. G. Reinhard, Phys. Rep. **309**, 117 (1999).
[37] M. V. Ammosov, N. B. Delone, and V. P. Krainov, Zh. Eksp. Teor. Fiz. **91**, 2008 (1986) [Sov. Phys. JETP **64**, 1191 (1986)].
[38] D. Wu, B. Qiao, X. T. He, C. McGuffey, and F. N. Beg, Phys. Plasmas **21**, 123118 (2014).
[39] D. Wu, X. T. He, W. Yu, and S. Fritzsche, Phys. Rev. E **95**, 023208 (2017).
[40] Refer to http://physics.nist.gov/PhysRefData/ASD/ for ionization energy data.
[41] G. Ecker and W. Kroll, Phys. Fluids **6**, 62 (1963).
[42] J. C. Stewart and K. D. Pyatt, Astrophys. J. **144**, 1203 (1966).
[43] J. Chihara, J. Phys.: Condensed Matter **3**, 8715 (1991).
[44] B. B. L. Witte, P. Sperling, M. French, V. Recoules, S. H. Glenzer, and R. Redmer, Phys. Plasmas **25**, 056901 (2018).
[45] B. Xu and S. X. Hu, Phys. Rev. E **84**, 016408 (2011).
[46] O. Gunnarsson and B. I. Lundqvist, Phys. Rev. B **13**, 4274 (1976).